## EDGE ARTICLE

Check for updates

# Multi-enzyme reaction inspired photocatalysis for solar-driven $CO_2$ reduction to ethane†

Qian Zhang,‡[a] Shuaiqi Gao,‡[a] Xiao Zhao,[b] Huiyong Wang, [ID] *[a] Yingying Guo,[a] Zhimin Liu [ID] *[c] and Jianji Wang [ID] *[ad]

Photocatalytic $CO_2$ reduction for the production of multicarbon products has emerged as a green and sustainable technology, which shows great potential and cost-effectiveness. However, photocatalytic synthesis of two-carbon ($C_2$) compounds is quite challenging due to the high activation barrier of the C−C coupling reaction and low content of intermediates. Herein, inspired by the tandem synthesis in multi-enzyme reactions, $Cu-N_4$ and $Mo-N_4$ active sites have been designed and integrated in CuPor-POP-Mo as cascade dual metal sites for efficient photocatalytic reduction of $CO_2$ to ethane ($C_2H_6$) for the first time. Significantly, an excellent $C_2H_6$ production rate of 472.5 μmol $g^{-1}$ $h^{-1}$ and a high product selectivity of 87.5% (electron selectivity ∼97.5%) have been achieved, which are the record high values in photocatalytic $C_2H_6$ production by using porous polymer catalysts. *In situ* spectral characterization studies and DFT calculations indicate that the Cu site enhanced the localized surface coverage of *CO on CuPor-POP-Mo, while the Mo site of the photocatalyst triggered the C−C coupling of *CO intermediates, and the energy barrier of which was synergistically lowered by Cu and Mo sites, resulting in highly effective $C_2H_6$ production. This work develops novel metal sites for ethane production and enables precise modulation of *CO intermediate coverage to decrease the energy barrier for *OCCO generation, thus opening a new pathway for highly selective photocatalytic $CO_2$ reduction toward value-added chemicals and fuels.

## Introduction

Ethane ($C_2H_6$) is one of the desirable gases in many industrial fields due to its wide applications as a fuel, refrigerant, and raw material or synthetic intermediate of organic compounds. Traditionally, $C_2H_6$ is mainly produced from natural gas separation and petroleum cracking.[1] These processes are characterized by energy intensive and high carbon emissions, which cause many energy and ecological environment problems. Therefore, seeking new and sustainable $C_2H_6$ production technologies is urgently needed in the framework of carbon neutrality. Solar-driven photoreduction of $CO_2$ into $C_2H_6$ is promising since only $CO_2$, water and clean solar energy are being utilized, and the reactions can be performed under ambient conditions.[2] However, the reported products in the photocatalytic $CO_2$ reduction reaction ($CO_2$RR) are mainly $C_1$ products (*e.g.*, CO, $CH_4$, and HCOOH),[3,4] while $C_2$ and multi-carbon ($C_{2+}$) products, especially $C_2H_6$, are rarely reported[5–9] at the current stage.

In biological systems, $CO_2$ reduction to $C_{2+}$ products is achieved by enzyme catalytic reactions, which can be seen as a tandem process enabled by two or more enzymes where each enzyme catalyses a specific step in the $CO_2$RR.[10,11] Importantly, to achieve the goals of high yield and high selectivity, the multi-enzyme catalytic reactions need to be well regulated in living organisms for an efficient metabolic process to increase the intermediates' concentrations and facilitate their C−C coupling. Compartmentalization is common in living organisms to manipulate the multi-enzyme reactions, which refers to the isolation of multi-enzymes or enzyme systems with tandem reaction feature into different compartments.[12] One typical example of compartmentalization can be found in chloroplast, where three-dimensional granum is evolved for loading enzyme/pigment relevant to water splitting and oxygen evolution, while the enzyme for the Calvin cycle ($CO_2$ fixation) is

[a]*Key Laboratory of Green Chemical Media and Reactions (Ministry of Education), Collaborative Innovation Centre of Henan Province for Green Manufacturing of Fine Chemicals, School of Chemistry and Chemical Engineering, Henan Normal University, Xinxiang, Henan, 453007, P. R. China. E-mail: jwang@htu.edu.cn; hywang@htu.edu.cn*

[b]*Science and Technology on Aerospace Chemical Power Laboratory, Hubei Institute of Aerospace Chemotechnolgy, Hubei, 441003, P. R. China*

[c]*Beijing National Laboratory for Molecular Sciences, Key Laboratory of Colloid, Interface and Thermodynamics, CAS Research/Education Centre for Excellence in Molecular Sciences, Institute of Chemistry, Chinese Academy of Sciences, Beijing, 100190, P. R. China. E-mail: liuzm@iccas.ac.cn*

[d]*College of Chemistry and Molecular Sciences, Longzihu New Energy Laboratory, Henan University, Zhengzhou, 450000, P. R. China*

† Electronic supplementary information (ESI) available. See DOI: https://doi.org/10.1039/d5sc03323c

‡ These authors contributed equally to this work.

confined in the chloroplast stroma.[13] The confined space in cell membranes benefits the enrichment of intermediates around the $CO_2$ fixation enzymes. These biological phenomena enlighten us to rationally analyse the production process of the $C_2H_6$ product.

Generally, C–C coupling between *CO intermediates is the rate-determining step for the formation of $C_2$ and $C_{2+}$ products.[8] Thus, the coverage of *CO and the stability of the *OCCO intermediate (from C–C coupling) on the catalytic sites are critically important for $C_2H_6$ formation. Regarding these two key factors, the stability of the *OCCO intermediate ensures the C–C coupling to produce $C_2H_6$, whereas the high coverage of *CO promotes the kinetics of the C–C coupling reaction. According to the multi-enzyme catalytic reactions for $CO_2$ fixation mentioned above, these two steps can be regarded as a kind of tandem process, where the first step is the stabilization and enrichment of the $C_1$ intermediates (such as *CO and *COOH), and the second step is the C–C coupling reaction between the $C_1$ intermediates. Therefore, for high yield and high selectivity production of $C_2H_6$, cascade photocatalysts (one for the first step, and the other for the second step) must be designed to integrate the isolated dual catalytic sites separated by compartmentalization. Porous organic polymers (POPs) have been considered as a new class of promising candidate cascade photocatalysts for $CO_2$ reduction featuring high structural designability and excellent chemical stability. In particular, metalloporphyrin-based POPs not only can stabilize M–N$_4$ (M = Co, Ni, Cu, and Fe) active sites but also can moderately anchor another metal site into the extended framework structure, thereby forming adjacent and stable dual-site structures. However, almost all the reduction products are $C_1$ compounds because most of the POPs used contain a single-metal active center, which is unfavorable for the C–C coupling.[14–18] To our knowledge, no studies on the photocatalytic production of $C_2$ and $C_{2+}$ products have been reported by using POP catalysts.

Herein, we designed and synthesized porous organic polymers (POPs) loaded with isolated Cu and Mo dual metal sites (CuPor-POP-Mo) as cascade photocatalysts for efficient $C_2H_6$

production (Fig. 1). Benefiting from the unique structure, the as-constructed CuPor-POP-Mo showed excellent $CO_2$RR performance with a $C_2H_6$ production rate of 472.5 μmol g$^{-1}$ h$^{-1}$ and a product selectivity of 87.5% (electron selectivity ∼97.5%), which represent the record high values in both production rate and selectivity for $C_2H_6$ production under the catalysis of porous polymer materials such as metal organic frameworks (MOFs), metal incorporating covalent organic frameworks (COFs) and POPs. Furthermore, control experiments and in/ex situ spectral characterization studies were performed, together with theoretical simulations, to explore the roles of different metal ions in the photocatalytic $CO_2$RR to $C_2H_6$. It was found that the Mo site was mainly responsible for the C–C coupling, while the Cu site enhanced the surface coverage of *CO on the CuPor-POP-Mo, and synergistically lowered the energy barriers of *OCCO formation with the Mo site. Thus, an interesting mechanism was proposed for Cu- and Mo-site cascade photocatalytic $CO_2$ reduction.

## Results and discussion

### Synthesis and characterization

CuPor-POP-Mo with Cu and Mo dual isolated metal sites was prepared by a hydrothermal approach (shown in Fig. 1). For this purpose, 5,10,15,20-tetrakis(4-aminophenyl)-21H,23H-porphine (Por) and Cu(OAc)$_2$ were first used to prepare Cu-Por, which was then reacted with 5,5′,5″-(benzene-1,3,5-triyl)tripicolinaldehyde (TTPD) in a mixture of 1,3,5-trimethylbenzene, 1,4-dioxane and 6 M AcOH at 120 °C for 96 h to produce porous polymer CuPor-POP as an insoluble powder. Then, the mixture of MoCl$_5$, 2,2′-bipyridin and CuPor-POP was refluxed at 95 °C for 24 h under a nitrogen atmosphere to fabricate bimetallic porous polymer CuPor-POP-Mo. For comparison studies, Mo incorporating porous porphine polymer Por-POP-Mo was also synthesized by the reaction of 5,10,15,20-tetrakis(4-aminophenyl)-21H,23H-porphine with TTPD and MoCl$_5$. The detailed synthetic procedures for the above materials are described in the ESI.†
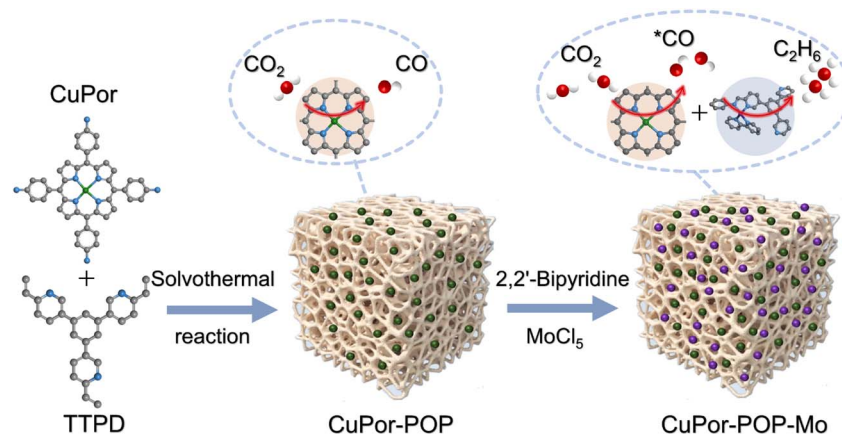


Fig. 1 Schematic illustration for the synthesis of CuPor–POP–Mo and photocatalytic $CO_2$ reduction. Here, the amine monomer is 5,10,15,20-tetrakis(4-aminophenyl)-21H,23H-porphine-Cu(II) (CuPor), and the aldehyde monomer is 5,5′,5″-(benzene-1,3,5-triyl)tripicolinaldehyde (TTPD).

The chemical structures of CuPor-POP, Por-POP-Mo and CuPor-POP-Mo were characterized by Fourier transform infrared (FT-IR) spectroscopy (Fig. S1†). The appearance of the peak at 999 cm$^{-1}$, which is assigned to the Cu–N (pyrrolic) bond,[19] demonstrates the existence of the Cu-porphyrin moiety in CuPor-POP (Fig. S1A and B†). The disappearance of the –C=O stretching peak at 1699 cm$^{-1}$ in the starting aldehyde[20] and –N=H stretching peaks at 3204–3353 cm$^{-1}$ in the amine monomer,[21] along with the appearance of a new peak attributed to the –C=N stretching vibration at 1603 cm$^{-1}$ in Cu-Por-POP,[22] indicates the successful formation of imine linkage. Upon incorporation of Mo into CuPor-POP, the peaks of the imine –C=N bond (1599 cm$^{-1}$)[23,24] and pyridine –C=N bond (1374 cm$^{-1}$)[25] show a redshift, which provides evidence for the coordination of Mo toward N atoms of the imine and pyridine groups[26] in CuPor-POP-Mo (Fig. S1B†). Additionally, the peaks of the imine –C=N (1598 cm$^{-1}$) and pyridine –C=N (1374 cm$^{-1}$) in Por-POP-Mo also exhibit a redshift related to Por-POP, indicating Mo coordination with N atoms of imine and pyridine groups (Fig. S1C and D†). Solid-state $^{13}$C NMR spectroscopy confirmed the formation of the –C=N bond in CuPor-POP, Por-POP-Mo and CuPor-POP-Mo with a characteristic carbon signal at 158.1 ppm (Fig. S2†).[27] As shown in Fig. S3,† the broad peaks in the powder X-ray diffraction (XRD) patterns of CuPor-POP, Por-POP-Mo and CuPor-POP-Mo indicate that these POPs all have amorphous structures. This is similar to that of the amorphous POPs containing imine groups reported in the literature.[28] Moreover, the diffraction peaks related to the metal salts or metal nanoparticles were not found, suggesting the absence of metal salts and metal nanoparticles in the POPs.

The surface area and porosity of the POPs were assessed by nitrogen adsorption–desorption measurements at 77 K, and the results are presented in Fig. S4.† The BET surface area was found to be 148, 121 and 41 m$^2$ g$^{-1}$ for CuPor-POP, Por-POP-Mo and CuPor-POP-Mo, respectively. As we expected, the introduction of Mo into CuPor-POP resulted in a significant decrease in the BET surface area of CuPor-POP-Mo. The well-developed porous structures for the as-prepared POPs implied the accessible catalytic sites and the facilitated mass transfer, which are beneficial for catalysis efficiency. In addition, we also determined CO$_2$ adsorption isotherms on the POPs at 25 °C to identify their affinity to CO$_2$ (Fig. S5†). The CO$_2$ adsorption capacity of CuPor-POP, Por-POP-Mo and CuPor-POP-Mo was 8.6, 13.0 and 15.8 cm$^3$ g$^{-1}$, respectively. Obviously, the addition of Mo in CuPor-POP almost doubled the adsorption capacity of CO$_2$ over CuPor-POP-Mo, which indicates that the Mo atom can effectively increase the CO$_2$ adsorption capacity and would be favorable for the photocatalytic CO$_2$RR.[20] Thermal gravimetric analysis (TGA) curves (Fig. S6†) of CuPor-POP, Por-POP-Mo and CuPor-POP-Mo suggested their high thermal stability up to 250 °C. The scanning electron microscopy (SEM) images showed that the spherical morphology of the POPs was intact after loading metal ions (Fig. S7†). The corresponding transmission electron microscopy (TEM) image again confirmed the absence of metal nanoparticles of different sizes in CuPor-POP-Mo (Fig. S8†). Moreover, the energy-dispersive X-ray spectrum (EDS) mapping images revealed that Cu and Mo atoms were

distributed uniformly on the surface of CuPor-POP and CuPor-POP-Mo (Fig. S9–S11†). The content of copper and molybdenum atoms in the POPs was determined by inductively coupled plasma-mass spectrometry (ICP-MS). It was found that the Cu atom content in CuPor-POP was 10.9 wt%, Mo atom content in Por-POP-Mo was 13.2 wt%, while the Cu and Mo contents in CuPor-POP-Mo were 8.5 and 11.9 wt%, respectively. It should be noted that, unless otherwise specified, CuPor-POP-Mo in the next discussion refers to the bimetallic POP catalyst with this composition.

To confirm the local microenvironment and chemical state of Cu and Mo in the POPs, X-ray photoelectron spectrum (XPS), Fourier transform extended X-ray absorption fine structure (FT-EXAFS) spectrum and X-ray absorption near-edge structure (XANES) spectrum measurements were performed. It can be seen from Fig. 2A and S12† that the N 1s peak in the XPS spectrum of CuPor-POP could be deconvoluted into three peaks: one at 399.7 eV for pyrrolic–N–Cu, one at 399.0 eV for C–N and one at 398.3 eV for pyridinic-N.[29,30] Por-POP exhibited typical pyrrolic-N (399.5 eV), C–N (399.0 eV), pyridinic-N (398.3 eV) peaks and CuPor exhibited typical pyrrolic–N–Cu (399.7 eV), and C–N (398.7 eV) peaks (Fig. S12C and D†). These XPS results suggested that Cu ions in CuPor-POP could form coordination bonds with the nitrogen atom in the porphyrin centre. The disappearance of the pyrrolic-H peak (at −2.75 ppm) in the $^1$H NMR spectrum of CuPor further verified that the Cu was coordinated in the centre of the porphyrin group[30] (Fig. S13†). In the Cu 2p XPS spectrum of CuPor and CuPor-POP, one peak at 934.2 eV was assigned to Cu$^{2+}$ (ref. 31–33) (Fig. 2B and S12E†). Additionally, the satellite peaks at 942.3, 942.5, 963.0 and 963.3 eV were observed for CuPor and CuPor-POP, respectively.[34,35] This suggested that copper in CuPor and CuPor-POP mainly existed as Cu$^{2+}$ rather than Cu$^0$ and Cu$^+$. Similarly, the peak assigned to Cu$^{2+}$ was also observed at 934.5 eV in CuPor-POP-Mo, which indicated that the valence state of Cu species in CuPor-POP-Mo was the same as that in CuPor-POP. Importantly, for CuPor-POP-Mo, the +0.3 eV shift of Cu 2p binding energy compared to CuPor-POP and the −0.1 eV shift of Mo 3d binding energy relative to Por-POP-Mo indicated the charge redistribution between Cu and Mo and a successful construction of the coordination bond between CuPor-POP and the Mo ion.[36,37] To understand the electron transfer process between Cu and Mo at the molecular level, the Bader charge values of Cu and Mo sites in CuPor-POP, Por-POP-Mo and CuPor-POP-Mo were calculated by density functional theory (DFT) simulation (as shown in Fig. S14†). The Bader charge of the Cu atom in CuPor-POP and the Mo atom in Por-POP-Mo was 9.983 $e$ and 12.657 $e$, while that of Cu and Mo atoms in CuPor-POP-Mo was 9.889 $e$ and 12.753 $e$, respectively. This result confirmed the charge redistribution between Cu and Mo. Furthermore, compared with the N 1s spectrum of CuPor-POP, an obvious positive shift of the N 1s peak in CuPor-POP-Mo was detected (Fig. 2C), which could have resulted from the formation of the pyridinic–N–Mo coordinate bond.[38–40] It was noted from Fig. 2D that the Mo 3d$_{5/2}$ peak could be divided into two peaks located at 231.1 and 232.7 eV, indicating that the valence state of Mo in CuPor-POP-Mo was mainly 5+ (ref. 41 and 42) with a small
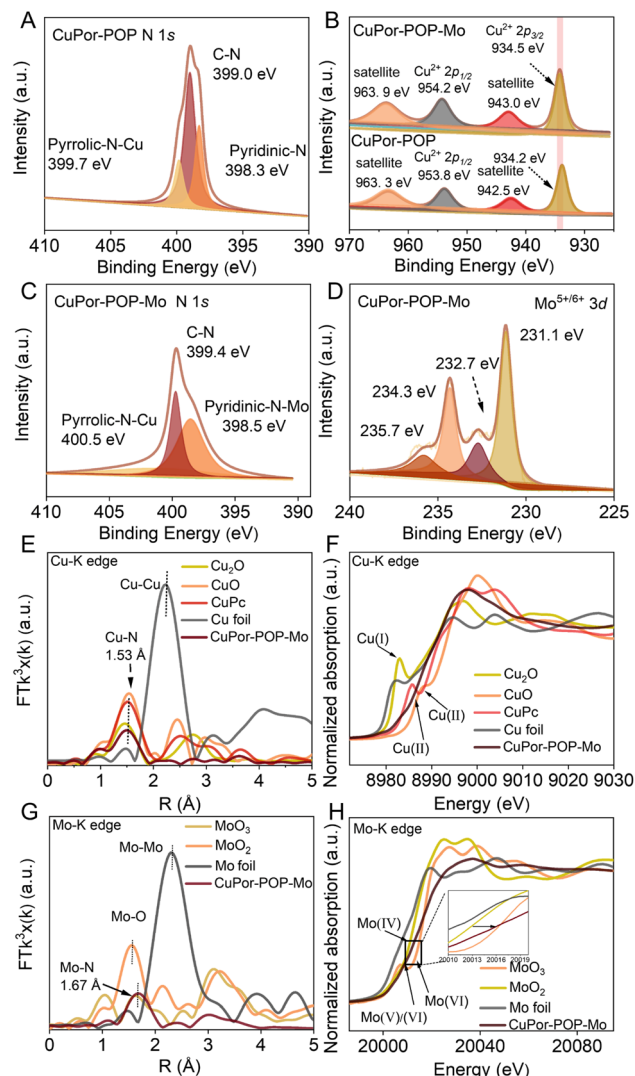
Fig. 2 Coordination environment analysis. (A) High-resolution N 1s XPS spectra of CuPor-POP. (B) High-resolution Cu 2p XPS spectra of CuPor-POP and CuPor-POP-Mo. (C) High-resolution N 1s XPS spectra of CuPor-POP-Mo. (D) High-resolution Mo 3d XPS spectra of CuPor-POP-Mo. (E and F) FT-EXAFS spectra and the normalized XANES spectra at the Cu K-edge of CuPor-POP-Mo, $Cu_2O$, CuO, CuPc and Cu foil samples. (G and H) FT-EXAFS spectra and the normalized XANES spectra at the Mo K-edge of CuPor-POP-Mo, $MoO_2$, $MoO_3$ and Mo foil samples.

amount of +6, which resulted from partial oxidation of a handful of $Mo^{5+}$ by air in the material preparation process. Similarly, the local microenvironment and chemical state of Mo in Por-POP-Mo were the same as those in CuPor-POP-Mo (Fig. S15†).

Fig. 2E–H show the FT-EXAFS and XANES spectra of CuPor-POP-Mo and the relevant reference materials. It can be seen from Fig. 2E that the Cu peak at 1.53 Å in the Cu K-edge EXAFS spectrum of CuPor-POP-Mo was close to that of CuPc (1.5 Å), implying the presence of the N-coordinated atomically dispersed Cu site,[8] which is in agreement with the XPS result. Meanwhile, the absence of the peak at 2.2 Å, ascribed to the Cu–Cu metallic bonds[8] (copper foil) in CuPor-POP-Mo, further

confirmed the atomically dispersed Cu site. Fig. 2F exhibits the Cu K-edge XANES spectrum of CuPor-POP-Mo as well as that of Cu foil, CuPc, $Cu_2O$ and CuO references. Notably, the near-edge absorption peak of CuPor-POP-Mo was located at the position corresponding to CuO. Additionally, the Mo K-edge EXAFS spectrum of CuPor-POP-Mo only displayed a prominent peak at 1.67 Å, corresponding to the N-coordinated atomically dispersed Mo site (Fig. 2G), which is in line with the result from the N 1s XPS of CuPor-POP-Mo. However, no peak was observed at 2.3 Å attributed to the Mo–Mo peak,[43,44] which also indicates the absence of any Mo clusters or nanoparticles in CuPor-POP-Mo. The Mo K-edge XANES spectra of CuPor-POP-Mo, Mo foil, $MoO_3$ and $MoO_2$ are shown in Fig. 2H. The absorption edge of CuPor-POP-Mo was situated between that of $MoO_2$ and $MoO_3$ while close to that of $MoO_3$, suggesting that the oxidation state of Mo in CuPor-POP-Mo was between +5 and +6, agreeing well with the XPS analysis of Mo species in CuPor-POP-Mo.[45]

The wavelet transform (WT) image further demonstrated the atomic dispersion of Cu and Mo in CuPor-POP-Mo in comparison with the standard samples (Fig. S16 and S17†). It was found that the atomic dispersion of Cu in CuPor-POP-Mo was much similar to that in CuPc, while the atomic dispersion of Mo in CuPor-POP-Mo was very different from that in $MoO_2$, $MoO_3$, and Mo foil. Combining with the results of XPS mentioned above, the formation of Mo–O and Mo–Mo bonds[25,46,47] could be excluded in CuPor-POP-Mo. The specific coordination number and microenvironments around the Cu and Mo centres were investigated by fitting the EXAFS data to the first coordination shell of CuPor-POP-Mo (Fig. S18 and Table S1†). It was noted that each Cu and Mo ion was coordinated by four N atoms (Cu–$N_4$ and Mo–$N_4$), and the average bond length of Cu–N and Mo–N was 2.02 and 2.12 Å, respectively, in the first shell. According to the atom content of N, Cu and Mo in CuPor-POP-Mo determined by XPS results, the molar ratio of N to (Cu + Mo) was 4.26, which suggested that CuPor-POP-Mo can provide sufficient active sites for each Cu and Mo atom to form Cu–$N_4$ and Mo–$N_4$ coordinate structures (Table S2†).[48,49] Therefore, Mo and Cu ions in CuPor-POP-Mo were mainly coordinated with N atoms to form Cu–$N_4$ (all N from the porphyrin centre) and Mo–$N_4$ (1 N from imine, 1 N from TTPD, and 2 N from 2,2′-bipyridine) sites.

## Optical characteristics and photocatalytic performance

The light-harvesting capability and band gap structures of CuPor-POP, Por-POP-Mo and CuPor-POP-Mo were investigated to understand the influence of Cu and Mo dual metal sites on the intrinsic photocatalytic properties. As shown in Fig. S19,† the absorption edge of all the POPs in solid-state ultraviolet-visible (UV-vis) diffuse reflection spectra was larger than 700 nm, indicating that they could be directly used in visible light photocatalysis.[31] Compared with CuPor-POP and Por-POP-Mo, the absorption edge of CuPor-POP-Mo showed a redshift due to electron delocalization caused by the dual metal sites, which is more beneficial to visible light photocatalytic reaction. Based on the Tauc plots obtained from the Kubelka–Munk equation (Fig. S20†), the optical band gap ($E_g$) of the samples was calculated to be 1.82, 1.78, and 1.65 eV for CuPor-POP, Por-

POP-Mo, and CuPor-POP-Mo, respectively. Obviously, CuPor-POP-Mo had a smaller band gap than that of CuPor-POP and Por-POP-Mo, which is more accessible for electron transfer from the valence band (VB) to conduction band (CB). As shown in the Mott–Schottky plots (Fig. S21†), CuPor-POP, CuPor-POP-Mo and Por-POP-Mo were n-type semiconductors with typical positive slopes, and the CB edge at pH = 7 was −0.71, −0.68, and −0.77 V (vs. the normal hydrogen electrode (NHE)), respectively. The CB value of these POPs was lower than the redox potential of $CO_2$ to CO (−0.53 V), $CH_4$ (−0.24 V), $C_2H_4$ (0.06 V) and $C_2H_6$ (−0.27 V),[8,36] and much higher than the lowest unoccupied molecular orbital energy level (−1.31 V vs. NHE) of the photosensitizer $[Ru(bpy)_3]Cl_2$.[20] Based on the equation $E_g = E_{VB} − E_{CB}$, the VB position of CuPor-POP, Por-POP-Mo and CuPor-POP-Mo was computed to be 1.11, 1.01, and 0.97 V, respectively, which are very close to those obtained from XPS spectra (Fig. S22†). Thus, it is clear that the photocatalytic reduction of $CO_2$ was thermodynamically favorable, and the transfer of photo-

induction generated electrons of $[Ru(bpy)_3]Cl_2$ was feasible with the POPs (Fig. S23†).

To evaluate the photocatalytic $CO_2$ reduction performance of CuPor-POP-Mo, photocatalytic measurements were performed in acetonitrile (MeCN)/water mixed solution under visible light irradiation by using $[Ru(bpy)_3]Cl_2$ and triethanolamine (TEOA) as the photosensitizer and electron donor, respectively. For the purpose of comparison, the catalytic performance of CuPor-POP and Por-POP-Mo was also evaluated under the same conditions. First, a series of control experiments were conducted for CuPor-POP-Mo, and the detailed results are presented in Fig. 3A. It can be seen that the $CO_2$ photoreduction reaction did not take place under the conditions without visible light, TEOA, or $[Ru(bpy)_3]Cl_2$. In the test without catalyst, only a minor amount of $H_2$ was detected. As shown in Fig. 3B, under visible light irradiation, $C_2H_6$ was the main product in the presence of CuPor-POP-Mo, and low $C_2H_6$ production rate and selectivity were observed with Por-POP-Mo as the catalyst, but $C_2H_6$ was almost undetectable in the presence of CuPor-POP, as determined by gas
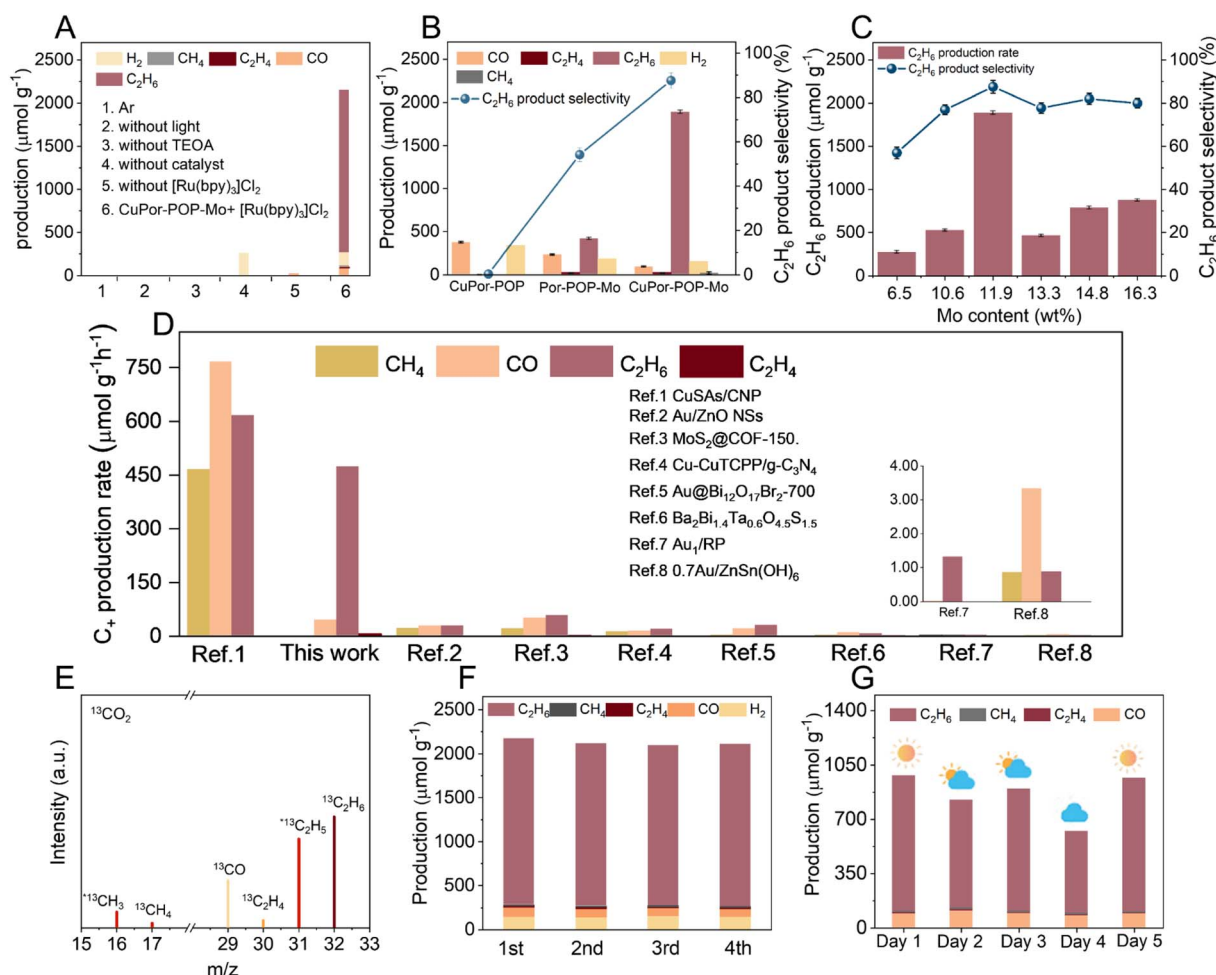


Fig. 3 The photocatalytic performance of CuPor-POP-Mo under 4 hours of visible light irradiation. (A) Control experiments for the selection of catalytic conditions. (B) Photocatalytic $CO_2$ reduction products over the as-synthesized photocatalysts. (C) Production of $C_2H_6$ under CuPor-POP-Mo catalysis with different masses of Mo. (D) Comparison of the gas products produced from the photocatalytic $CO_2$RR using CuPor-POP-Mo as the catalyst with those reported in recent literature. (E) Result of gas chromatography-mass spectrometry with the $^{13}C$ isotope tracer. (F) Production of $CO_2$ reduction products during the stability tests using CuPor-POP-Mo as the catalyst. (G) Performance tested under natural sunlight (test duration: 4 hours per day).

chromatography (GC) (Fig. S24†). For all POPs, no liquid products were detected by $^1H$ NMR spectroscopy (Fig. S25†). The above results indicated that in the bimetallic CuPor-POP-Mo photocatalyst, the Mo site was decisive for the production of $C_2H_6$ through the C–C coupling reaction, while the Cu site accelerated the kinetics of the C–C coupling reaction. Thus, the Cu and Mo dual metal sites in CuPor-POP-Mo synergistically promoted $C_2H_6$ production from $CO_2$ photoreduction.

Then, to obtain the optimal production rate and selectivity of $C_2H_6$, the effect of the content of Mo in CuPor-POP-Mo and the catalyst dosage used in the reaction on catalytic performance was investigated, where the content of Cu in CuPor-POP-Mo was fixed (8.5 wt%). As shown in Fig. 3C, the production rate and selectivity of $C_2H_6$ first increased and then decreased with the increase of the Mo mass. When the Cu and Mo contents in CuPor-POP-Mo were 8.5 and 11.9 wt%, respectively, the catalytic performance was best for the $CO_2RR$ to $C_2H_6$. Moreover, it was found that when the dosage of CuPor-POP-Mo used in the reaction was 5 mg and the volume ratio of MeCN/water reached 29.5 : 0.5, the highest selectivity and production rate of $C_2H_6$ were obtained (Fig. S26†). Surprisingly, under these optimal conditions, CuPor-POP-Mo exhibited an excellent $C_2H_6$ production rate of 472.5 μmol $g^{-1}$ $h^{-1}$ and high product selectivity of 87.5% (electron selectivity of 97.5%), and the production rate was about 3 times that of Por-POP-Mo. To our knowledge, both production rate and selectivity of $C_2H_6$ reported here are record high values in photocatalytic $C_2H_6$ production by using porous polymer catalysts (Fig. 3D and Table S3†). Under such conditions, the accompanied by-products were CO, $H_2$, $CH_4$ and $C_2H_4$, and their production rate was 11, 37.5, 2.5 and 5 μmol $g^{-1}$ $h^{-1}$, respectively. To verify the carbon origin of $C_2H_6$, we utilized the $^{13}C$ isotope-labeled $CO_2$ as the substrate for the $CO_2RR$, and the reacted gas mixture was detected by gas chromatography-mass spectrometry (GC-MS). Major signals with $m/z$ values of 16, 17, 29, 30, 31 and 32 assigned to $*^{13}CH_3$, $^{13}CH_4$, $^{13}CO$, $^{13}C_2H_4$, $*^{13}C_2H_5$ and $^{13}C_2H_6$, respectively, were detected when $^{13}CO_2$ is used as feedstock for the photocatalytic $CO_2RR$ by GC-MS (Fig. 3E), confirming that the generated hydrocarbon was from $CO_2$ rather than the other organic molecules.

The apparent quantum efficiency (AQE) for the $CO_2RR$ to $C_2H_6$ under the catalysis of CuPor-POP-Mo was then studied at various wavelengths. As shown in Fig. S27 and Table S4,† when the AQE values of CuPor-POP-Mo were plotted against the absorption wavelength of $[Ru(bpy)_3]Cl_2$, the data points fell nicely on its optical absorption spectrum curve. The highest AQE value was determined to be 0.55% at 450 nm. This result confirmed that $[Ru(bpy)_3]Cl_2$ functioned as the photosensitizer in the present work. Furthermore, long-term stability of the photocatalyst was investigated due to its particular importance in practical applications. For the CuPor-POP-Mo catalyst, no significant decrease in $C_2H_6$ production rate was observed after the fourth cycle (Fig. 3F), demonstrating good cycling stability of this photocatalyst. In addition, the composition and structure of the CuPor-POP-Mo could be well maintained, as confirmed by comparing its TEM images, FTIR spectra, PXRD patterns, and XPS spectra before and after recycling (Fig. S28 and S29†).

In terms of the practical application of CuPor-POP-Mo, natural sunlight irradiation was also used for the photocatalytic $CO_2RR$ to $C_2H_6$ under the reaction conditions similar to those mentioned above. For this purpose, a 4 h photocatalytic reaction (from 10:00 am to 02:00 pm) per day was conducted outdoors in our campus for 5 consecutive days in December as described previously.[20] Remarkably, the average production rate and selectivity of $C_2H_6$ reached 218 μmol $g^{-1}$ $h^{-1}$ and 81.3%, respectively (Fig. 3G). Considering the lower temperature (approximately 21 °C) and weaker light intensity (less than 50 mW $cm^{-2}$) during testing (Table S5†), such a high production rate and selectivity for $C_2H_6$ demonstrated the advantages of CuPor-POP-Mo in the photocatalytic $CO_2RR$ to $C_2H_6$. This result highlights the great potential of the synergistic dual isolated metal site strategy in the design of cascade photocatalysts for practical applications.

## Reaction mechanism

The photo-generated electron–hole separation efficiency and photo-generated electron transfer capacity of CuPor-POP-Mo were also studied to explain why the dual metal sites showed outstanding performance in the photocatalytic $CO_2RR$ to $C_2H_6$. As shown in Fig. S30,† CuPor-POP-Mo exhibited much higher transient photocurrent density than CuPor-POP and Por-POP-Mo due to the synergistic effect of Cu and Mo on the separation of photo-generated electron–hole pairs. At the same time, the electrochemical impedance spectra (EIS) of the samples also manifested that the transfer of photo-generated electrons in CuPor-POP-Mo was much faster than that in CuPor-POP and Por-POP-Mo, as judged by the smaller semicircle in Nyquist plots (Fig. S31†). Moreover, the steady-state PL spectra and PL decay spectra were measured to evaluate the separation ability of the catalysts for photo-generated electrons–holes (Fig. S32†). By fitting the curves with a biexponential equation,[25] the average lifetime ($\tau_{avg}$) of photo-generated electrons on CuPor-POP, Por-POP-Mo and CuPor-POP-Mo was computed to be 2.85, 3.65 and 3.82 ns, respectively. Clearly, the lifetime of photogenerated electrons over CuPor-POP-Mo was longer than that over CuPor-POP and Por-POP-Mo, which was beneficial for improving photocatalytic performance. This result indicated that dual metal sites of Cu and Mo in CuPor-POP-Mo played an important role in the enhancement of photogenerated electron–hole separation efficiency under light irradiation. In addition, steady-state PL spectra (Fig. S33†) suggested that the strong emission of the photosensitizer $[Ru(bpy)_3]Cl_2$ was effectively quenched by CuPor-POP, Por-POP-Mo and CuPor-POP-Mo, but CuPor-POP-Mo exhibited the most pronounced PL quenching effect, which led to a shorter electron excitation lifetime of $[Ru(bpy)_3]Cl_2$ (160 ns).[26] This phenomenon disclosed that the recombination of photo-generated electron and hole pairs of $[Ru(bpy)_3]Cl_2$ was better prevented by CuPor-POP-Mo, and long-lived electrons were provided for $CO_2$ reduction, resulting in enhanced $CO_2$ photo-reduction efficiency.

The charge carrier process in excited state dynamics was further analyzed using femtosecond transient absorption (fs-TA) spectra (Fig. S34†). Under 365 nm pump light excitation,

$[Ru(bpy)_3]Cl_2$ showed a negative ground-state bleaching peak at around 450 nm, which suggested the excitation of electrons in $[Ru(bpy)_3]Cl_2$. Meanwhile, when CuPor-POP, Por-POP-Mo or CuPor-POP-Mo was added into the solution of $[Ru(bpy)_3]Cl_2$, the peak with a positive signal of excited state absorption at around 600 nm was observed, which was attributed to the transfer of the excited electrons to Cu and Mo active sites[50] (Fig. S35 and Table S6†). These results confirmed that the introduction of Cu and Mo sites indeed accelerates the dynamic electron transfer process from $[Ru(bpy)_3]Cl_2$ to CuPor-POP-Mo. To acquire more evidence for the electron transfer in the photocatalytic reaction, quasi-*in situ* XPS measurements were conducted for the mixture of CuPor-POP-Mo with photosensitizer $[Ru(bpy)_3]Cl_2$. As shown in Fig. 4A, a positive shift of the Ru 3d binding energy occurred from 281.4 to 281.7 eV upon visible light irradiation, implying that the Ru ion in the photosensitizer lost electrons.[31] In comparison, the Cu 2p binding energy negatively shifted from 934.2 to 932.8 eV, and the Mo 3d binding energy also negatively shifted from 231.5 to 229.2 eV, manifesting that the Mo site had stronger electron capture ability than the Cu site (Fig. 4B and C).[8] However, the binding energy of C, N and Cl was not shifted after visible light irradiation (Fig. S36†). Consequently, it could be inferred that photogenerated electrons of the photosensitizer $[Ru(bpy)_3]Cl_2$ transferred to Mo and Cu ions upon visible

light irradiation and then the $CO_2RR$ took place on Cu and Mo sites of CuPor-POP-Mo as active centers. To gain a deeper understanding of the intrinsic relationship between the electronic structure of metal-based catalysts and their catalytic performance, the density of states (DOS) of the Cu active site in CuPor-POP and the Mo site in Por-POP-Mo was determined by DFT calculations. As shown in Fig. S37,† Mo possesses a higher DOS at the Fermi energy ($E_f$) level for d-orbitals, which was significantly higher than that for the d-orbitals of Cu. This result indicated that more electrons accumulated near the Fermi level of the Mo site compared with that of the Cu site, which was more beneficial to the photogenerated charge separation and transfer in Por-POP-Mo than that in CuPor-POP, resulting in higher catalytic activity of Por-POP-Mo.[51,52]

*In situ* Fourier transform infrared (FTIR) spectroscopy was used to detect the possible intermediates during $CO_2$ photoreduction to $C_2H_6$. As demonstrated in Fig. 4D and S38,† in the presence of $[Ru(bpy)_3]Cl_2$, the peaks of *COOH (1650 and 1699 $cm^{-1}$),[36,53] $H-CO_3^-$ (1421, 1434 and 1635 $cm^{-1}$),[36,54–56] m-$CO_3^{2-}$ (1362, 1506, 1522 and 1540 $cm^{-1}$),[56] b-$CO_3^{2-}$ (1285, 1558, 1619, 1671 and 1684 $cm^{-1}$),[36,56] p-$CO_3^{2-}$ (1393 $cm^{-1}$),[36] formate (1735, 1771 and 1794 $cm^{-1}$)[36,57] and the absorbed *CO (1717 and 2064 $cm^{-1}$)[8,58–60] were observed in the *in situ* FTIR spectrum of CuPor-POP, but the $C_2$-related intermediates were not detected.



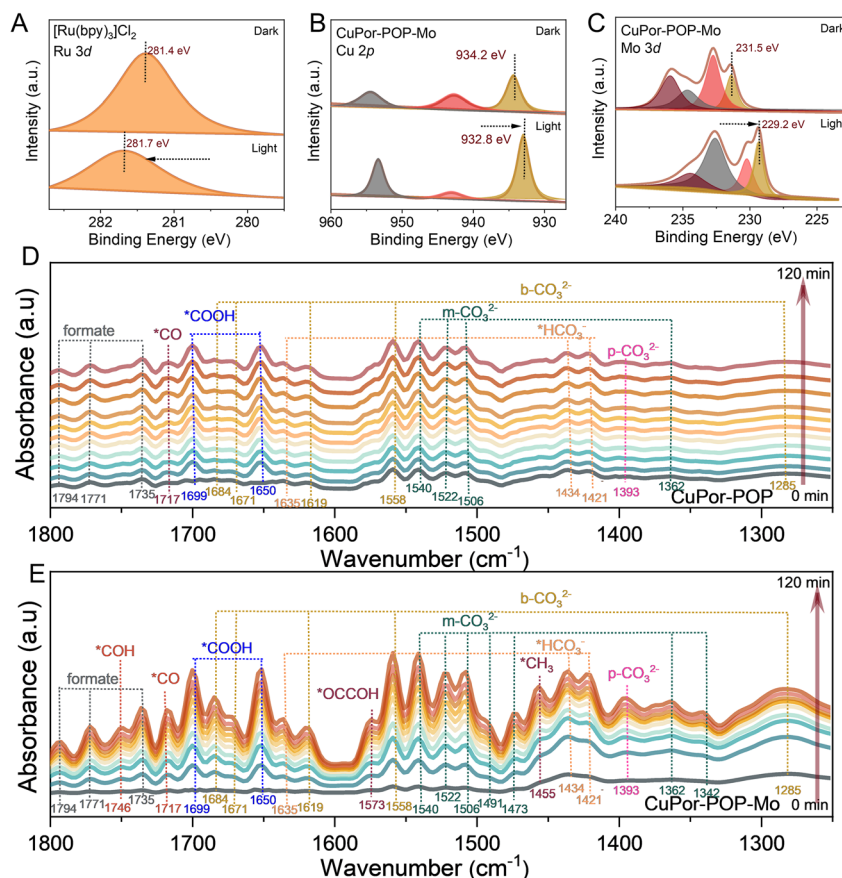**Fig. 4** Quasi-*in situ* XPS spectra and *in situ* ATR–FTIR spectra. Quasi-*in situ* XPS spectra of (A) Ru 3d, (B) Cu 2p and (C) Mo 3d for $[Ru(bpy)_3]Cl_2$ and CuPor-POP-Mo under light and in the dark. Room temperature *in situ* ATR–FTIR spectra of (D) CuPor-POP and (E) CuPor-POP-Mo for the detection of intermediates during $CO_2$ photoreduction.

However, in the spectrum of Por-POP-Mo and CuPor-POP-Mo, the peaks for *COH (1746 cm$^{-1}$),[61,62] *OCCOH (intermediate after hydrogenation of *OCCO, 1573 cm$^{-1}$)[6,60,63] and *CO (2064 and 1717 cm$^{-1}$)[60] occurred (Fig. 4E, S39 and S40†). Notably, significant peaks of *COH, *OCCOH and *CO were observed in the *in situ* FTIR spectrum of CuPor-POP-Mo (Fig. 4E and S40†). To quantitatively compare the relative content of the *CO intermediate produced on Por-POP-Mo and CuPor-POP-Mo, the peak area of this intermediate was normalized based on the approach reported in the literature,[64,65] and the results are summarized in Table S7.† It was found that with the extension of the photocatalytic reaction time to 120 min, the peak area of *CO increased from 0.01 to 2.1 on Por-POP-Mo, and from 0.01 to 2.7 on CuPor-POP-Mo, implying that the introduction of Cu in Por-POP-Mo increased *CO coverage on POPs. Moreover, the peak area of *COH and *OCCOH on CuPor-POP-Mo was also much higher than that on Por-POP-Mo after photocatalytic reduction of 120 min (Table S8 and Fig. S41†). In addition, significant vibration peaks of *CH$_3$ (C$_2$H$_6$) and *CH$_2$ (C$_2$H$_4$) were also observed at 1455/2960/2874 and 2924/2819 cm$^{-1}$ respectively, in the *in situ* FTIR spectrum of CuPor-POP-Mo,[8,66-68] and their intensity increased with prolonged CO$_2$ reduction time, which indicated that more C$_2$H$_6$ was formed. To exclude the interferences of the photosensitizer, sacrificial agent (TEOA) and photocatalyst, *in situ* FTIR measurement with $^{13}$CO$_2$ as feedstock was conducted, and the same reaction intermediates were also observed and redshift of the corresponding peaks was evidenced (Fig. S42†). These results strongly support the conclusion drawn from the above photocatalytic experiments that the C–C coupling was mainly triggered by the Mo site, while the Cu site readily enhanced the *CO coverage, and promoted the C–C coupling reaction. This is quite different from the electrocatalytic CO$_2$RR to C$_{2+}$ products for the Cu site reported in the literature.[6,8]

Based on the intermediates detected by *in situ* FTIR spectroscopy, we performed DFT calculations to understand the mechanism of the dual-metal site photocatalytic CO$_2$RR to C$_2$H$_6$ in these optimized structural models. First, charge density difference (CDD) and electron localization function (ELF) were calculated to describe the interaction of *CO with metal sites in the photocatalyst. For the purpose of comparison, the same structural fragment in CuPor-POP, Por-POP-Mo and CuPor-POP-Mo was considered. It can be seen from Fig. 5A that there was a minor electron accumulation and depletion between *CO and the Cu site, indicating that *CO weakly interacted with the Cu site.[69] However, significant electron accumulation and depletion were found between *CO and the Mo site (Fig. 5B and C), suggesting a stronger interaction between the Mo site and *CO. Notably, the *CO interaction with the Cu site is weaker than with the Mo site, indicating that the *CO enables favoring spontaneous spill over from Cu to Mo sites in thermodynamics. The preferential interaction with *CO at the Mo surface ultimately drives the localized *CO coverage on CuPor-POP-Mo.[70] Furthermore, the related DFT calculations were conducted for the reaction pathway of the CO$_2$RR to CO over CuPor-POP, Por-POP-Mo and CuPor-POP-Mo. As shown in Fig. S43,† all these catalysts had the potential to convert CO$_2$ into CO due to the

negative Δ*G* values. However, Δ*G* value change in the desorption of *CO decreased in the order: Por-POP-Mo (2.22 eV) > CuPor-POP-Mo (0.85 eV) > CuPor-POP (−0.26 eV). This means that the Cu site mainly catalyzed the formation of *CO, but the *CO intermediate was not stable on the Cu site and easily escaped from this site. This is the reason why C–C coupling could not be completed on CuPor-POP. By contrast, the Mo site in CuPor-POP-Mo suitably stabilized the *CO intermediate, thus triggering C–C coupling reactions to form C$_2$ products.

Based on the *in situ* FTIR results, both *CO and *OCCOH (hydrogenation of *OCCO) intermediates were detected during the photocatalytic CO$_2$RR. Then, we optimized the free energy diagram for the CO$_2$RR to C$_2$H$_6$ over CuPor-POP-Mo and Por-POP-Mo from *CO and focused on the formation of the *OCCO intermediate. It was found that under favourable energy conditions, *CO intermediates underwent a C–C coupling process to form the *OCCO intermediate, and then through the continuous hydrogenation process, the CH$_2$COH intermediate was generated, which was followed by either C–O bond breaking to form *CH$_2$C (ethylene pathway)[71,72] or C–H bond formation to produce *CH$_3$COH (ethane pathway). Then, the interaction between as-synthesized POPs and reaction intermediates, including *CO, *OCCO, *OCCOH, *CHOCHO, *CHOHCOH, *CH$_2$OHCOH, *CH$_2$COH, *CH$_3$COH, *CH$_3$CHOH, *CH$_3$CH$_2$OH and *CH$_3$CH$_3$, was carefully studied by DFT calculation (Fig. 5D and S44†). It can be found that the important intermediates, such as *OCCO, *CHOHCOH, *CH$_2$COH, and *CH$_3$COH, were stabilized by both Cu and Mo sites through Cu–O (O atom from intermediates) and Mo–C (C atom from intermediates) interactions, respectively. As a result, the free energy levels of these reaction intermediates for CuPor-POP-Mo were all lower than that of Por-POP-Mo (Fig. 5D). Moreover, the change of Δ*G* value from *CH$_2$COH to *CH$_3$COH formation was more negative than from *CH$_2$COH to *CH$_2$C on Por-POP-Mo and CuPor-POP-Mo, indicating a more favourable process for ethane production than the ethylene pathway. These results revealed that the dual metal sites in CuPor-POP-Mo: Mo site were mainly responsible for the C–C coupling and improving the selectivity of C$_2$H$_6$ through the interaction between the Mo atom and C atom (from key intermediates), while the Cu site enhanced the surface coverage of *CO on the CuPor-POP-Mo and synergistically lowered the energy barriers of *OCCO formation with the Mo site through the interaction between the Cu atom and O atom. Thus, Cu and Mo sites synergistically facilitate the generation of the C$_2$H$_6$ product. Based on the above experimental and theoretical results, a detailed mechanism was proposed for the CO$_2$ photoreduction to C$_2$H$_6$ catalyzed by CuPor-POP-Mo. Upon visible light irradiation, the photosensitizer [Ru(bpy)$_3$]Cl$_2$ is excited to produce electrons. The irregular porosity and electron delocalization of POPs would be beneficial to the quick transfer of the excited state electrons to the Cu and Mo sites of CuPor-POP-Mo. Then, CO$_2$ is reduced to *CO on the dual metals and large amounts of *CO on the Cu site are spilled over into the Mo site to increase the coverage of *CO and ensured *CO stability on the catalyst, and subsequently *OCCO intermediates are formed on the Mo site by C–C coupling in coordination with the Cu site. Finally, the *OCCO intermediate is continuously
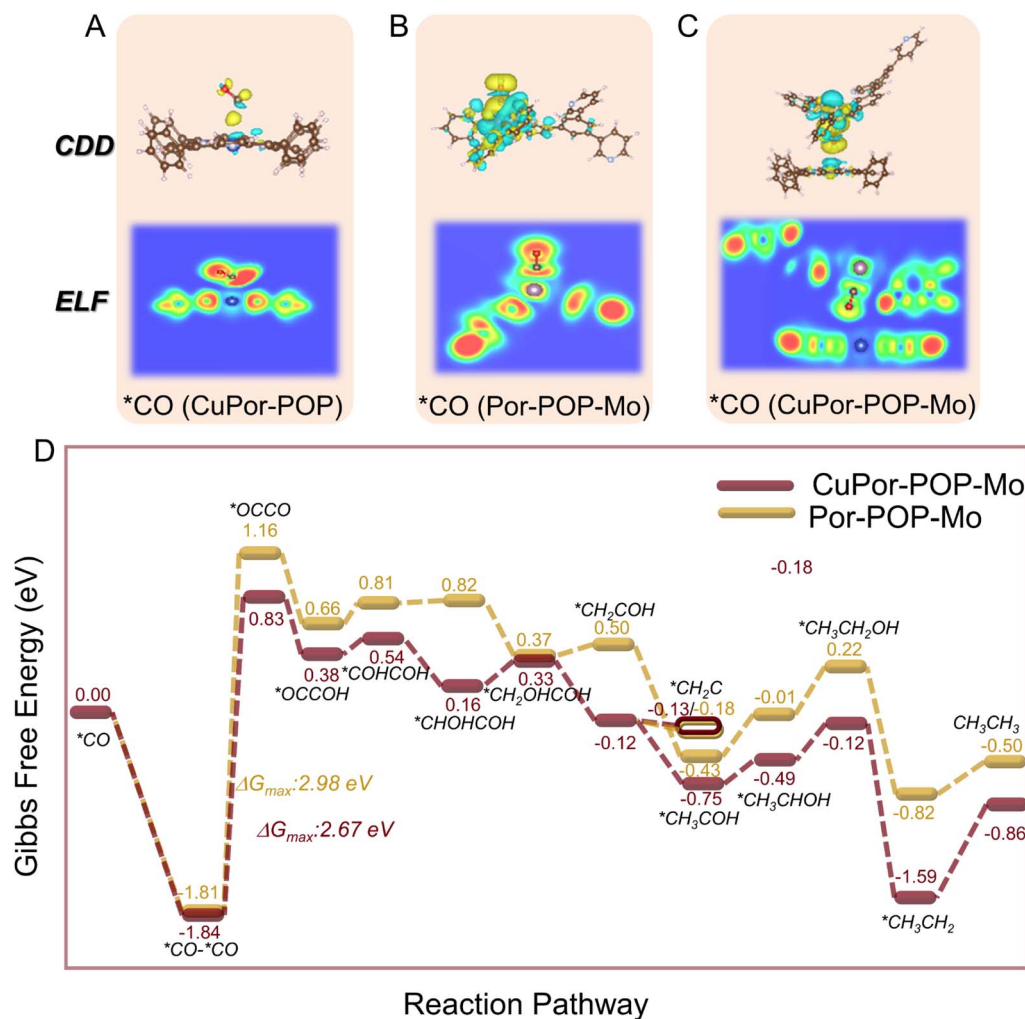
Fig. 5 The density functional theory (DFT) calculations and reaction Gibbs free energy change. Charge density difference (yellow and cyan areas with an isosurface value of 0.0005 indicate charge accumulation and depletion, respectively). Carbon atoms are presented as light brown, O atoms as red, Cu atoms as dark blue, N atoms as light blue, and Mo atoms as purple in (A) CuPor-POP, (B) Por-POP-Mo, and (C) CuPor-POP-Mo. Electron localization function where red and blue areas indicate electron localization and electron delocalization, respectively, in CuPor-POP, Por-POP-Mo, and CuPor-POP-Mo. (D) Gibbs free energy profiles of the $CO_2RR$ to $C_2H_6$ over CuPor-POP-Mo and Por-POP-Mo. The "*" represents adsorption on the substrate.

hydrogenated and deoxidized to $C_2H_6$ with the help of Mo and Cu sites. The remaining holes are captured by the electron donor TEOA, which is then oxidized to $TEOA_{ox+}$, and the entire cycle is closed.

## Conclusions

In summary, CuPor-POP-Mo with Cu and Mo dual isolated sites was successfully designed to effectively catalyze the photochemical conversion of $CO_2$ to $C_2H_6$. After irradiation with visible light for 4 h, a $C_2H_6$ production rate of 472.5 μmol $g^{-1}$ $h^{-1}$ and a product selectivity of 87.5% (electron selectivity ∼97.5%) were achieved, which appear to surpass that of most photocatalysts reported previously. Even under natural sunlight, an average $C_2H_6$ production rate of 218 μmol $g^{-1}$ $h^{-1}$ and product selectivity of 81.3% could be attained. The superior photocatalytic performance was ascribed to the synergistic

effect of Cu and Mo sites to promote electron transfer and suppress the photo-generated electron–hole recombination. *In situ* IFTS measurements and DFT calculations suggest that the formation of *OCCO species on the Mo site from *CO–*CO coupling was the rate-determining step for the photoreduction of $CO_2$ into $C_2H_6$. The introduction of the Cu site substantially improved the surface coverage of *CO on CuPor-POP-Mo, and synergistically decreased the energy barrier of C–C coupling which appeared on the Mo site of the photocatalyst. This work provides new insights into the rational design of cascade catalysts for $CO_2$ photoreduction to hydrocarbon fuels with high activity and selectivity.

## Data availability

The data that support the findings of this study are available in the paper and ESI.† Source data are provided with this paper.

## Author contributions

J. J. W., Z. M. L., H. Y. W., and Q. Z. designed the experiments. Q. Z. and S. Q. G. performed the experiments and analysed the data. Y. Y. G. completed some synthesis experiments. X. Z. provided the DFT calculation support. Q. Z., H. Y. W., J. J. W and Z. M. L. wrote the manuscript. All authors discussed the results and commented on the manuscript.

## Conflicts of interest

The authors declare no competing interests.

## Acknowledgements

## References

1 J. Albero, Y. Peng and H. García, *ACS Catal.*, 2020, **10**, 5734–5749.

2 W. Gao, H. Q. Chi, Y. J. Xiong, J. H. Ye, Z. G. Zou and Y. Zhou, *Adv. Funct. Mater.*, 2023, **34**, 2312056.

3 K. K. Sakimoto, A. B. Wong and P. Yang, *Science*, 2016, **351**, 74–77.

4 I. Roh, S. Yu, C. K. Lin, S. Louisia, S. Cestellos Blanco and P. Yang, *J. Am. Chem. Soc.*, 2022, **144**, 8002–8006.

5 J. Fan, L. Cheng, J. Fan, Q. Wang, M. Gao, D. Li and J. Feng, *J. CO2 Util.*, 2023, **67**, 102333.

6 B. Zhou, Y. Ma, P. Ou, Z. Ye, X. Y. Li, S. Vanka, T. Ma, H. Sun, P. Wang, P. Zhou, J. K. Cooper, Y. Xiao, I. A. Navid, J. Pan, J. Song and Z. Mi, *Nat. Catal.*, 2023, **6**, 987–995.

7 J. Jia, Y. Luo, H. Wu, Y. Wang, X. Jia, J. Wan, Y. Dang, G. Liu, H. Xie and Y. Zhang, *J. Colloid Interface Sci.*, 2024, **658**, 966–975.

8 G. Wang, Z. Chen, T. Wang, D. Wang and J. Mao, *Angew. Chem., Int. Ed.*, 2022, **61**, e202210789.

9 S. Sorcar, Y. Hwang, J. Lee, H. Kim, K. M. Grimes, C. A. Grimes, J. W. Jung, C. H. Cho, T. Majima and M. R. Hoffmann, *Energy Environ. Sci.*, 2019, **12**, 2685–2696.

10 Z. Li, Y. Yang, Z. Yin, X. Wei, H. Peng, K. Lyu, F. Wei, L. Xiao, G. Wang, H. D. Abruña, J. Lu and L. Zhuang, *ACS Catal.*, 2021, **11**, 2473–2482.

11 L. Xu, P. Trogadas and M.-O. Coppens, *Adv. Energy Mater.*, 2023, **13**, 2302974.

12 R. J. R. W. Peters, M. Marguet, S. Marais, M. W. Fraaije, J. C. M. van Hest and S. Lecommandoux, *Angew. Chem., Int. Ed.*, 2014, **53**, 146–150.

13 L. Zhang, J. Shi, Z. Jiang, Y. Jiang, S. Qiao, J. Li, R. Wang, R. Meng, Y. Zhu and Y. Zheng, *Green Chem.*, 2011, **13**, 300–306.

14 W. Zhao, D. Zhai, C. Liu, D. Zheng, H. Wu, L. Sun, Z. Li, T. Yu, W. Zhou, X. Fang, S. Zhai, K. Han, Z. He and W. Q. Deng, *Appl. Catal., B*, 2022, **300**, 120719.

15 D. K. Nandi, J. Seth, P. Chakrabortty, S. Ghosh, A. Chowdhury, A. Bhaumik and S. M. Islam, *ChemCatChem*, 2023, **15**, e202301018.

16 M. Du, Z. Wu, X. Zhang, X. Song, Y. Zhao, W. Xue, H. Huang and J. Li, *Chem. Eng. J.*, 2024, **500**, 157157.

17 A. Boruah, B. Boro, R. Paul, C.-C. Chang, S. Mandal, A. Shrotri, C.-W. Pao, B. K. Mai and J. Mondal, *ACS Appl. Mater. Interfaces*, 2024, **16**, 34437–34449.

18 M. Wang, G. Zhang, S. Dong, N. Li, Q. Xu, H. Li, J. Lu and D. Chen, *Adv. Funct. Mater.*, 2024, **34**, 2406516.

19 Z. Su, L. Ma, J. Wei, X. Bai, N. Wang and J. Li, *Appl. Organomet. Chem.*, 2022, **36**, e6632.

20 Q. Zhang, S. Gao, Y. Guo, H. Wang, J. Wei, X. Su, H. Zhang, Z. Liu and J. Wang, *Nat. Commun.*, 2023, **14**, 1147.

21 Q. Zhu, Y. Zheng, Z. Zhang and Y. Chen, *Nat. Protoc.*, 2023, **18**, 3080–3125.

22 X. Liu, H. Li, W. Zhang, Z. Yang, D. Li, M. Liu, K. Jin, L. Wang and G. Yu, *Angew. Chem., Int. Ed.*, 2023, **62**, e202308921.

23 W. Xu, S. Zhou, B. Wang, P. Zhang and K. Tang, *Sep. Purif. Technol.*, 2022, **288**, 120646.

24 W. G. Leng, Y. S. Peng, J. Q. Zhang, H. Lu, X. Feng, R. L. Ge, B. Dong, B. Wang, X. P. Hu and Y. A. Gao, *Chem.–Eur. J.*, 2016, **22**, 9087–9091.

25 L. Ran, Z. Li, B. Ran, J. Cao, Y. Zhao, T. Shao, Y. Song, M. K. H. Leung, L. Sun and J. Hou, *J. Am. Chem. Soc.*, 2022, **144**, 17097–17109.

26 Y. Song, J. J. Zhang, Z. H. Zhu, X. Chen, L. B. Huang, J. J. Su, Z. T. Xu, T. H. Ly, C. S. Lee, B. I. Yakobson, B. Z. Tang and R. Q. Ye, *Appl. Catal., B*, 2021, **284**, 119750.

27 S. Lin, C. S. Diercks, Y. B. Zhang, N. Kornienko, E. M. Nichols, Y. Zhao, A. R. Paris, D. Kim, P. Yang, O. M. Yaghi and C. J. Chang, *Science*, 2015, **349**, 1208–1213.

28 X. H. Ma, C. H. Pang, S. H. Li, Y. H. Xiong, J. P. Li, J. H. Luo and Y. Yang, *Biosens. Bioelectron.*, 2019, **146**, 111734.

29 M. Xiao, J. Zhu, L. Ma, Z. Jin, J. Ge, X. Deng, Y. Hou, Q. He, J. Li, Q. Jia, S. Mukerjee, R. Yang, Z. Jiang, D. Su, C. Liu and W. Xing, *ACS Catal.*, 2018, **8**, 2824–2832.

30 F. Lv, M. Sun, Y. Hu, J. Xu, W. Huang, N. Han, B. Huang and Y. Li, *Energy Environ. Sci.*, 2023, **16**, 201–209.

31 J. Zhou, J. Li, L. Kan, L. Zhang, Q. Huang, Y. Yan, Y. Chen, J. Liu, S. L. Li and Y. Q. Lan, *Nat. Commun.*, 2022, **13**, 4681.

32 R. J. Wei, H. G. Zhou, Z. Y. Zhang, G. H. Ning and D. Li, *CCS Chem.*, 2020, **3**, 2045–2053.

33 H. B. Aiyappa, J. Thote, D. B. Shinde, R. Banerjee and S. Kurungot, *Chem. Mater.*, 2016, **28**, 4375–4379.

34 Q. Fang, J. Wen, H. Wang, X. Wei, L. Jiao, X. Luo, M. Sha, Y. Qin, M. Liu, L. Zheng, W. Gu, H. Zhong, L. Hu and C. Zhu, *Nano Energy*, 2024, **131**, 110217.

35 G. D. Khattak, A. Mekki and M. A. Gondal, *Appl. Surf. Sci.*, 2010, **256**, 3630–3635.

36 M. Kou, W. Liu, Y. Wang, J. Huang, Y. Chen, Y. Zhou, Y. Chen, M. Ma, K. Lei, H. Xie, P. K. Wong and L. Ye, *Appl. Catal., B*, 2021, **291**, 120146.

37 X. Zhang, H. Sun, Y.-R. Wang, Z. Shi, R.-L. Zhong, C.-Y. Sun, J.-Y. Liu, Z.-M. Su and Y.-Q. Lan, *Adv. Mater.*, 2024, **36**, 2408510.

38 D. Wang, T. Liu, J. Wang and Z. Wu, *Carbon*, 2018, **139**, 845–852.

39 H. Lin, S. Li, G. Yang, K. Zhang, D. Tang, Y. Su, Y. Li, S. Luo, K. Chang and J. Ye, *Adv. Funct. Mater.*, 2021, **31**, 2007071.

40 S. Kuramochi, A. Fiorani and Y. Einaga, *Diam. Relat. Mater.*, 2023, **139**, 110277.

41 X. Li, G. Zhang, Y. Chang, Q. Cui, M. Zhang, W. Zou and M. Zhou, *Chem. Eng. J.*, 2024, **499**, 156337.

42 P. Du, K. Hu, J. Lyu, H. Li, X. Lin, G. Xie, X. Liu, Y. Ito and H.-J. Qiu, *Appl. Catal., B*, 2020, **276**, 119172.

43 Z. Chen, F. An, Y. Zhang, Z. Liang, W. Liu and M. Xing, *Proc. Natl. Acad. Sci. U. S. A.*, 2023, **120**, e2305933120.

44 Y. Wang, G. Jia, X. Cui, X. Zhao, Q. Zhang, L. Gu, L. Zheng, L. H. Li, Q. Wu, D. J. Singh, D. Matsumura, T. Tsuji, Y.-T. Cui, J. Zhao and W. Zheng, *Chem*, 2021, **7**, 436–449.

45 Y. N. Gong, W. Zhong, Y. Li, Y. Qiu, L. Zheng, J. Jiang and H. L. Jiang, *J. Am. Chem. Soc.*, 2020, **142**, 16723–16731.

46 R. Chen, Y. Wang, Y. Ma, A. Mal, X.-Y. Gao, L. Gao, L. Qiao, X.-B. Li, L.-Z. Wu and C. Wang, *Nat. Commun.*, 2021, **12**, 1354.

47 L. Zhang, X. Chu, L. Liu, S. Zhang, H. Liu, Y. Li, X. Zhang, S. Song and H. Zhang, *Adv. Funct. Mater.*, 2024, **35**, 2413043.

48 Y. Su, Q. Mu, N. Fan, Z. Wei, W. Pan, Z. Zheng, D. Song, H. Sun, Y. Lian, B. Xu, W. Yang, Z. Deng and Y. Peng, *Small*, 2024, **20**, 2312020.

49 X. Zhang, J. Chen, G. Wang, Y. Dong, J. Ji, L. Li, M. Xue and H.-M. Cheng, *Angew. Chem., Int. Ed.*, 2024, **64**, e202416367.

50 L. J. Gong, L. Y. Liu, S. S. Zhao, S. L. Yang, D. H. Si, Q. J. Wu, Q. Wu, Y. B. Huang and R. Cao, *Chem. Eng. J.*, 2023, **458**, 141360.

51 X. Zhu, X. Yuan, M. Ge and Y. Tang, *Small*, 2024, **20**, 2405158.

52 S. Chen, F. Huang, L. Mao, Z. Zhang, H. Lin, Q. Yuan, X. Lu and J. Shi, *Nano-Micro Lett.*, 2024, **17**, 32.

53 X. Y. Dong, Y. N. Si, Q. Y. Wang, S. Wang and S. Q. Zang, *Adv. Mater.*, 2021, **33**, 2101568.

54 D. Guo, Y. Lu, Y. Ruan, Y. Zhao, Y. Zhao, S. Wang and X. Ma, *Appl. Catal., B*, 2020, **277**, 119278.

55 X. Cai, X. Sui, J. Xu, A. Tang, X. Liu, M. Chen and Y. Zhu, *CCS Chem.*, 2021, **3**, 408–420.

56 J. X. Cui, Y. M. Fu, B. Meng, J. Zhou, Z. Y. Zhou, S. M. Liu and Z. M. Su, *J. Mater. Chem. A*, 2022, **10**, 13418–13427.

57 X. Yang, X. Lan, Y. Zhang, H. Li and G. Bai, *Appl. Catal., B*, 2023, **325**, 122393.

58 N. Li, B. Wang, Y. Si, F. Xue, J. Zhou, Y. Lu and M. Liu, *ACS Catal.*, 2019, **9**, 5590–5602.

59 M. Liu, Q. Wang, T. Luo, M. Herran, X. Cao, W. Liao, L. Zhu, H. Li, A. Stefancu, Y. R. Lu, T. S. Chan, E. Pensa, C. Ma, S. Zhang, R. Xiao and E. Cortés, *J. Am. Chem. Soc.*, 2024, **146**, 468–475.

60 J. Li, H. Huang, W. Xue, K. Sun, X. Song, C. Wu, L. Nie, Y. Li, C. Liu, Y. Pan, H.-L. Jiang, D. Mei and C. Zhong, *Nat. Catal.*, 2021, **4**, 719–729.

61 F. Xu, Z. Li, R. Zhu, Y. Chu, Z. Pan, S. Xia, J. Fu, Z. Xiao, X. Ji, M. Liu and B. Weng, *Appl. Catal., B*, 2022, **316**, 121615.

62 R. Xu, D.-H. Si, S.-S. Zhao, Q.-J. Wu, X.-S. Wang, T.-F. Liu, H. Zhao, R. Cao and Y.-B. Huang, *J. Am. Chem. Soc.*, 2023, **145**, 8261–8270.

63 J. Fan, Y. Zhao, H. Du, L. Zheng, M. Gao, D. Li and J. Feng, *ACS Appl. Mater. Interfaces*, 2022, **14**, 26752–26765.

64 X. Wang, L. Shi, W. Ren, J. Li, Y. Liu, W. Fu, S. Wang, S. Yao, Y. Ji, K. Ji, L. Zhang, Z. Yang, J. Xie and Y.-M. Yan, *J. Energy Chem.*, 2024, **99**, 409–416.

65 Y. Liu, Z. Yue, C. Jin, L. Zheng, J. Shi, D. Li, Y. Wang, J. Bai, K. Leng, W. Wang, Y. Qu and Q. Li, *Small*, 2025, **21**, 2409259.

66 Y. Kim, S. Park, S.-J. Shin, W. Choi, B. K. Min, H. Kim, W. Kim and Y. J. Hwang, *Energy Environ. Sci.*, 2020, **13**, 4301–4311.

67 S. Zhu, T. Li, W.-B. Cai and M. Shao, *ACS Energy Lett.*, 2019, **4**, 682–689.

68 X. Li, S. Wang, L. Li, Y. Sun and Y. Xie, *J. Am. Chem. Soc.*, 2020, **142**, 9567–9581.

69 L. Lin, C. Hu, S. Xu, H. Jia, H. Tao and Z. Zhang, *Mater. Today Commun.*, 2022, **32**, 103681.

70 J. Li, Y. Chen, B. Yao, W. Yang, X. Cui, H. Liu, S. Dai, S. Xi, Z. Sun, W. Chen, Y. Qin, J. Wang, Q. He, C. Ling, D. Wang and Z. Zhang, *J. Am. Chem. Soc.*, 2024, **146**, 5693–5701.

71 R. Das, R. Paul, A. Parui, A. Shrotri, C. Atzori, K. A. Lomachenko, A. K. Singh, J. Mondal and S. C. Peter, *J. Am. Chem. Soc.*, 2023, **145**, 422–435.

72 K. Wang, Q. Li, X. Chen, Z. Li, Y.-F. Yang, T.-S. Zhang, H.-M. Shen, Q. Wang, B. Wang, Y. Zhang, J. Xia, H. Li and Y. She, *Appl. Catal., B*, 2025, **362**, 124765.